Journal of
Materials Chemistry A

PAPER

View Article Online
View Journal

Cite this: DOI: 10.1039/d6ta02416e

Polyaminoanthraquinone with modulated iminium electron delocalization for efficient electrochemical ammonium removal

Fei Yu,[ac] Tianjie Chen,[a] Jinfeng Chen,[b] Shuzhen Liang,[c] Peng Liu[e] and Jie Ma *[bcd]

Received 20th March 2026
Accepted 12th May 2026

DOI: 10.1039/d6ta02416e

rsc.li/materials-a

The development of organic electrode materials for capacitive deionization (CDI) is hindered by limited redox-active sites and sluggish ion kinetics. Herein, a protic-acid-mediated interfacial polymerization strategy is proposed to fabricate nanoscale protonated polyaminoanthraquinone (PAAQ), mitigating these limitations. The protonated imine groups (–NH–) on the PAAQ chains form $-NH_2^+-$ polarons, inducing extensive π-electron delocalization along the polymer backbone, which activates the latent redox sites and significantly boosts the electrochemical performance. In addition, leveraging the intrinsically low crystallinity of PAAQ, interfacial polymerization was coupled with agitation to disperse the aqueous oxidant template, yielding nanoparticles whose increased specific surface area increases the accessible active adsorption sites. The optimized PAAQ material delivers an exceptional NH_4^+ removal capacity of 120.43 mg g^{-1} and a high rate of 9.22 mg g^{-1} min^{-1}, surpassing most reported organic electrodes. The material also shows outstanding cycling performance, maintaining 84.1% of its original capacity after 50 CDI cycles. This work proposes a protonation-activated strategy that unlocks the latent redox sites of conjugated polymers and amplifies their electrochemical performance, providing valuable insights for the development of high-performance organic electrodes in CDI and related energy storage applications.

1. Introduction

With the expansion of agriculture, acceleration of industrialization, and population growth, ammonium nitrogen emissions causing ammonium ion (NH_4^+) pollution have become one of the important environmental problems facing the world.[1–3] Industrial activities, including metallurgy, chemical manufacturing, fertilizer production, and coking, as well as agricultural practices such as excessive use of fertilizers and discharge of livestock wastewater, are the primary sources of ammonium nitrogen pollution.[4,5] The discharge of wastewater containing ammonium nitrogen contributes to water eutrophication and leads to the formation of hazardous substances such as nitrites and nitrates.[6,7] Ammonia reclaimed from the environment is being re-envisioned as a strategic, renewable energy carrier, capitalizing on its high energy density, carbon-free nature, safety, and transport economy—benefits that go well beyond its historical use in fertilizers.[8–10] With a high volumetric hydrogen density (106 kg H_2 per m^3 as a liquid at 300 K and 1.0 MPa, compared to liquid hydrogen's 70 kg H_2 per m^3 at 20 K),[11] ammonia is easy to store and transport, making it a versatile medium. Thus, efficient ammonia recovery from aqueous environments holds significant importance for environmental protection and energy utilization.

Traditional ammonia recovery methods, such as ammonia stripping, chemical precipitation, oxidation, membrane filtration, biological treatment and so on, have limitations.[12,13] Ammonia stripping needs pH and temperature adjustments, posing air pollution and scaling risks. Struvite precipitation requires large amounts of magnesium and alkali, yielding low fertilizer output. Anaerobic ammonium oxidation has a long start-up period and is sensitive to environmental changes. Therefore, there's an urgent need for a pollution-free, cost-effective, and energy-efficient NH_4^+ capture technology. Capacitive deionization (CDI) is an energy-saving emerging water treatment technology that involves adsorbing ions onto electrodes under an applied DC voltage, which is easy to operate, sustainable, and reusable with electrodes.[14,15] It can also

---

[a] College of Oceanography and Ecological Science, Shanghai Ocean University, No 999, Huchenghuan Road, Shanghai, 201306, P. R. China
[b] Research Center for Environmental Functional Materials, State Key Laboratory of Water Pollution Control and Green Resource Recycling, College of Environmental Science and Engineering, Tongji University, Shanghai, 200092, P. R. China
[c] Water Resources and Water Environment Engineering Technology Center, Xinjiang Key Laboratory of Engineering Materials and Structural Safety, School of Civil Engineering, Kashi University, Kashi 844000, P. R. China
[d] Shanghai Institute of Pollution Control and Ecological Security, Shanghai, 200092, P.R. China
[e] Biolin (Shanghai) Trading Company Ltd, Rm 1205, Sandhill Plaza, Lane 2290 ZuChongzhi Road, Pudong New District, 201203 Shanghai, China

selectively remove different ions through electrode design.[16,17] Compared to the various limitations of traditional inorganic electrode materials, such as anodic corrosion and co-ion effect of carbon materials, poor conductivity and volume expansion of inorganic Faraday materials,[18–26] organic electrode materials, which achieve ion storage through functional groups with redox activity to avoid the above defects, have become a hot research topic in CDI electrode materials in recent years. These pseudocapacitive organic electrode materials rich in active sites such as carbonyl groups and Schiff bases have shown significant advantages in terms of high capacity, adjustability, stability, and low toxicity.[27–31]

Given their high theoretical charge-storage capacities, well-defined redox potentials, rapid kinetics, and structural diversity, quinones have been the subject of extensive electrochemical research. Their theoretically substantial specific capacity is competitive with lithium-ion systems.[32,33] 1-Aminoanthraquinone (AAQ), an inexpensive organic precursor that incorporates redox-active quinone units, can be polymerized into extensively π-conjugated architectures, thereby enhancing the overall charge density, which has been widely exploited for proton storage and cation batteries. However, most previous CDI studies have relied on quinone-based oligomers obtained through condensation reactions that aim to establish a nominally complete π-conjugated backbone. The resulting polymer frameworks are fragile and readily dissolved in flowing aqueous electrolytes, representing one of the bottlenecks in the research of organic electrodes.[34,35] In fact, a straightforward homopolymerization of AAQ directly affords a long-chain, robust polyaminoanthraquinone (PAAQ) framework that withstands aqueous environments under periodic electric fields. Yet this otherwise straightforward route has received scant attention because the homopolymer backbone cannot sustain long-range π-electron delocalization, and the majority of its redox-active sites remain electrochemically silent. Although the anthraquinone moieties possess an intramolecular π–π conjugated framework, the interunit p–π conjugation supplied by the bridging imine group (–NH–) introduces periodic disruptions that act as energetic barriers to electron delocalization along the PAAQ chains, leading to limited conductivity.

Recent investigations have demonstrated that protonation of these –NH– linkages by protic acids drives the formation of P-doped polaronic states that reorganize the charge distribution along the PAAQ chain, and the resulting PAAQ effectively extends π-electron delocalization across the entire conjugated architecture, thereby markedly enhancing macroscopic electrical conductivity.[36,37] The improvement of conductivity is expected to activate the redox sites on conjugated polymers to achieve higher electrochemical adsorption capacity.[38,39] Additionally, in a reaction environment containing protic acids, amino groups (–NH_2) are protonated to more reactive –NH_3^+, thereby promoting the continuous polymerization of monomers to increase the yield of long-range polymers.[40] It should also be emphasized that monomers and oxidants are usually soluble in different solvents. Compared with *in situ* polymerization in a single solvent, interfacial polymerization in multiple solvents usually achieves better results.[41] When two immiscible liquids form an interface, one of the liquid solvents contains a monomer. Due to the difference in chemical potential between two immiscible liquids at the interface, monomers can diffuse towards the interface and initiate polymerization, thereby achieving precise design of the polymer structure based on solvent soft templates.

In this work, a novel and convenient AAQ polymerization method was developed. By utilizing the interface aggregation strategy and the promoting effect of a protic acid, the protonated PAAQ exhibits satisfactory microstructure and capacitance. This method achieves enhanced conductivity and activated redox sites for conjugated polymers by protic acid regulation of electron delocalization, endowing them with excellent electrochemical performance. At 1.2 V, the adsorption capacity of enhanced PAAQ for NH_4^+ is as high as 120.43 mg g^{-1}, and the adsorption rate is 9.22 mg g^{-1} min^{-1}, significantly better than that of the undoped acid and structurally optimized control sample. A series of characterization results indicate that the C═O group is the redox adsorption site for NH_4^+, and microgravimetric monitoring by an electrochemical quartz crystal microbalance with dissipation (EQCM-D) further corroborates the reversibility of the ion adsorption/desorption process.

2. Experimental methods

2.1. Materials and chemicals

1-Amino anthraquinone (AAQ, ≥98%) was obtained from Shanghai Adamas Co., Ltd (Shanghai, China). Ammonium persulphate (APS, AR, ≥98%) was purchased from Shanghai Titan Scientific Co., Ltd (Shanghai, China). Acetonitrile (HPLC, 99.90%) was obtained from Shanghai Adamas Co., Ltd (Shanghai, China). Perchloric acid ($HClO_4$, GR, 70.0–72.0%) was purchased from Yonghua Chemical Co., Ltd (Jiangsu, China). Ethanol absolute (AR, ≥99.7%) was provided by Shanghai Lingfeng Chemical Reagents Co., Ltd (China).

Activated carbon (AC) powder was obtained from Shanghai Macklin Biochemical Co.Ltd (Shanghai, China). AC powder, carbon black (Shanghai Adamas Co., Ltd) and polyvinylidene fluoride (PVDF, Adamas, average $M_w \sim 534\,000$, RG) were combined at a weight ratio of 8 : 1 : 1, followed by the addition of several drops of 1-methyl-2-pyrrolidinone (NMP, ≥99.5%, Aladdin), and the mixture was stirred for more than 12 h. This slurry was evenly coated onto a carbon paper and subsequently dried under vacuum at 60 °C to obtain an AC electrode with a thickness of approximately 0.1 mm.

2.2. Synthesis of PAAQ

1.2780 g of APS was added to 20 mL of deionized water and sonicated to obtain a uniform APS solution. 0.3125 g ($n_{AAQ} : n_{APS} = 1 : 4$) of AAQ monomer and 40 mL of acetonitrile were added to a beaker, then 140 μL of $HClO_4$ was dripped and sonicated for 15 min to obtain a uniform orange yellow transparent solution. The APS solution was then slowly added dropwise at a rate of one drop every three seconds while the mixture was stirred at 300 rpm and maintained at 25 °C. The color of the solution gradually turned dark orange, and stirring was continued at room temperature for 48 h, resulting in the formation of a black precipitate. This solid product (denoted as PAAQ-PS) was collected by centrifugation, washed sequentially with ethanol and deionized water, and finally dried in a vacuum oven at 60 °C. In addition, two additional samples were prepared under otherwise identical conditions to highlight the roles of acid and stirring: PAAQ-S, which involved stirring but no addition of protic acid, and PAAQ-P, which involved the addition of a protic acid but no stirring during the dropwise addition and subsequent reaction.

2.3. Material characterization

Scanning electron microscopy (SEM, GeminiSEM 300, Germany), X-ray diffractometer (XRD, Rigaku Ultima IV, Japan), X-ray photoelectron spectroscopy (XPS, Thermo Scientific K-Alpha, America), Fourier transform infrared spectrometer (FTIR, iS10, America), thermogravimetric analysis (TGA, TGA-1000C, China), electrochemical workstation (PGSTAT302N, Swiss), Electrochemical Quartz Crystal Microbalance with Dissipation Monitoring (EQCM-D, Biolin, Swiss). Based on the N_2 adsorption/desorption isotherms tested on a Micromeritics ASAP 2460, the corresponding specific surface area (SSA) of the different materials was calculated by Brunauer–Emmett–Teller (BET) measurements. The pore size distributions were calculated by Barrett–Joyner–Halenda analysis (BJH).

2.4. Electrochemical measurements

The PAAQ material, CB, and PVDF were mixed at a mass ratio of 8 : 1 : 1 in NMP solution and stirred for 24 hours to obtain a homogeneous slurry. The slurry was evenly coated onto a carbon paper using a film applicator at a thickness of 1 μm. The coated area was then carefully scraped to define a well-defined electrode region of 1 cm × 1 cm. After vacuum drying at 60 °C to completely remove the solvent, the total mass of the dried active materials on the electrode was approximately 0.5 mg. The resulting PAAQ electrode was then ready for electrochemical tests.

Electrochemical tests were performed on a standard three-electrode system connected to an electrochemical workstation. The as-synthesized PAAQ, a platinum sheet, and a saturated Ag/AgCl electrode served as the working, counter, and reference electrodes, respectively.

The specific capacitance (C, F g^{-1}) was derived from the galvanostatic charge–discharge (GCD) curves using the following equation:

$$C = \frac{I\Delta t}{m\Delta V} \tag{1}$$

Among them, I (A) is the discharging current, Δt (s) is the discharging duration, ΔV (V) represents the voltage window, and m (g) refers to the mass of the active material on the electrode.

Electrochemical-impedance spectroscopy (EIS) of the working electrode was performed on a workstation over the frequency window 0.01 to 10^5 Hz. The spectra were analyzed and fitted with equivalent circuits using ZView 3.3 software. The diffusion coefficient of NH_4^+ was subsequently extracted from the fitted data *via* the relationship:[42]

$$D_{NH_4^+} = \frac{R^2T^2}{2A^2n^4F^4C^2\sigma^2} \tag{2}$$

Among them, R refers to the gas constant, 8.314 J K^{-1} mol^{-1}. T refers to the Kelvin temperature. If tested at room temperature of 25 °C, $T = 298.15$ K. A refers to the area of the electrode sheet in cm^2. n refers to the number of electrons transferred during the reaction process, F refers to the Faraday constant, 96 485 C mol^{-1}. σ refers to the Warburg coefficient, which is the slope of the line fitting Z' and $\omega^{-0.5}$. C refers to NH_4^+ concentration in mol L^{-1}.

2.5. CDI experiment

The PAAQ electrode for CDI tests was prepared following the same coating and drying procedure as described for the electrochemical tests, except that the coated region was 2 cm × 2 cm and the dried active material mass was approximately 2 mg. The CDI cell was assembled in a symmetric stack, comprising (from outside to center) fixed separators, gaskets, conductive sheets, electrode materials, anion exchange membranes (AEMs), chambers, cation exchange membranes (CEMs), and then the reverse order back to the outer fixed separators. PAAQ and AC served as the cathode and anode materials, respectively. For each test, a 40 mL volume of 10 mM NH_4Cl solution was circulated through the system at a flow rate of 20 mL min^{-1}. Prior to applying voltage, the system was flushed with both deionized water and the NH_4Cl solution to achieve physical adsorption equilibrium on the electrodes. The concentration of NH_4Cl, which exhibits a linear relationship with solution conductivity, was monitored indirectly by measuring conductivity every 10 seconds using a conductivity meter (LeiCi, DDSJ-319L). All experiments were conducted in a sequential batch mode with applied voltages ranging from 0.8 to 1.2 V.

The NH_4^+ removal behaviors of the CDI system were evaluated by NH_4^+ removal capacity (NRC, mg g^{-1}) and NH_4^+ removal rate (NRR, mg g^{-1} min^{-1}), which were calculated according to the following equations:

$$\mathrm{NRC} = \frac{(C_0 - C_e) \times V}{m} \tag{3}$$

$$\mathrm{NRR} = \frac{\mathrm{NRC}}{t} \tag{4}$$

where C_0 and C_e (mg L^{-1}) are the concentrations of NH_4^+ at initial and final stages, respectively; V (L) is the volume of NH_4Cl solution; m (g) represents the respective quality of the electrode; t (min) refers to adsorption time.

3. Results and discussion

3.1. Synthesis and characterization of PAAQ

The synthetic route to PAAQ is illustrated in Fig. 1a. AAQ monomers were initiated by a protic acid ($HClO_4$) and propagated with APS as the oxidant, yielding PAAQ chains composed

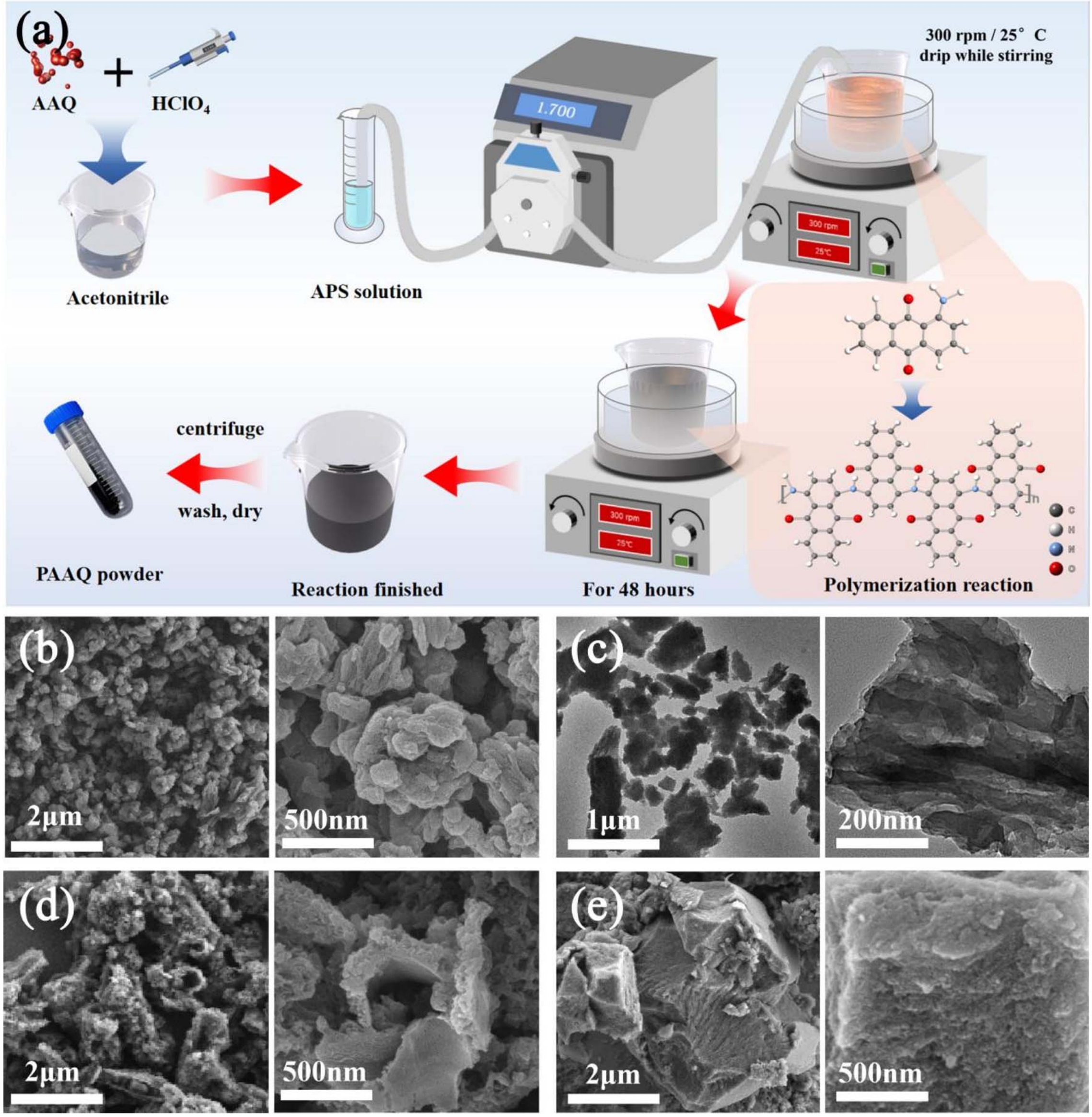

Fig. 1 Schematic diagram of the polymerization reaction of the PAAQ material (a), SEM (b) and TEM (c) images of PAAQ-PS, and SEM images of PAAQ-S (d) and PAAQ-P (e).

of –NH– linked repeat units. After 24 h of reaction, the initially dark-orange organic phase turned opaque-black, and a dense, black polymer film accumulated at the organic–water interface. To drive the conversion to completion, the reaction was prolonged to 48 h, after which an abundant black precipitate had settled at the interface. The crude product was isolated by centrifugation and purified *via* successive washes with absolute ethanol (until the supernatant became colorless) to remove unreacted AAQ, followed by deionized water to eliminate residual APS and neutralize residual acidity. The isolated PAAQ was obtained in 83.5% isolated yield. SEM coupled with EDS was employed to investigate the sample's morphology and elemental composition. As presented in Fig. S1, the EDS maps indicate a homogeneous dispersion of C, N, and O across the analyzed area. To investigate the promoting effect of the protic acid and the structural tunability enabled by interfacial polymerization, two control samples were prepared: (i) PAAQ-S (only stir), synthesized under neutral conditions with stirring, and (ii) PAAQ-P (only protic acid), prepared in the presence of a protic acid under static conditions. The sample prepared with simultaneous protic acid addition and stirring is denoted as PAAQ-PS.

Vigorous stirring dispersed the aqueous APS solution into acetonitrile, generating numerous nano-sized aqueous droplets that served as templates. At the resulting curved oil-water interface, AAQ monomers from the organic phase underwent oxidative polymerization, producing uniform polymer nanoparticles. As shown in the SEM image (Fig. 1b), the resulting PAAQ-PS material exhibits a well-dispersed, millet-like morphology. This was further confirmed by TEM (Fig. 1c), which revealed alternating dark and light contrast within individual grains, indicating thickness variations and confirming a three-dimensional porous architecture with abundant voids. This internal porosity provides essential pathways and a driving force for mass transport during the adsorption of water-based pollutants. In stark contrast, when the protic acid is omitted (PAAQ-S), polymerization is incomplete, affording irregular, sub-nano fragments resembling the wreckage of a sphere (Fig. 1d). The necessity of additional ethanol washes during purification corroborates the presence of a substantial amount of unreacted monomer, resulting in a markedly lower isolated yield (53.1%). It can therefore be concluded that protic acids augment the involvement of monomeric species in the polymerization reaction, thereby elevating the overall yield while simultaneously enforcing a template-directed propagation that secures the as-complete-as-possible growth of the polymer along the template, ultimately affording control over the polymer's microscopic morphology. Under static interfacial polymerization (PAAQ-P), the absence of mechanical agitation leads to coalescence of the aqueous APS phase, producing a dense bulk (Fig. 1e) whose compact architecture markedly differs from the small particulate morphology observed under stirring. Such dense packing is anticipated to hinder active site accessibility, underscoring the influence of stirring on the microstructural evolution of interface-polymerization organic polymer.

XRD patterns of the AAQ monomer and the corresponding polymer PAAQ are presented in Fig. 2a. The monomer exhibits a series of intense, well-defined Bragg reflections indicative of its high crystallinity. Upon oxidative polymerization, these sharp peaks collapse into broad, low-intensity humps centered at $2\theta = 25°$, which is the signature of π–π stacking between polymer backplanes.[35,43] XPS analysis revealed the elemental composition and bonding states of PAAQ. The high-resolution C 1s spectrum can be deconvoluted into four peaks centered at 284.8, 285.7, 287.5 and 290.3 eV, assigned to C–C/C=C, C–N, C=O and π–π stacking, respectively (Fig. 2b). Similarly, the N 1s spectrum (Fig. 2c) could be deconvoluted into three peaks at 399.4, 399.9 and 401.5 eV, corresponding to the quinonoid imine (=N–), amine (–NH–), and positively charged nitrogen (N^+) species.[44,45] The presence of the =N– component evidences an extended π-conjugation pathway between the lone pair on nitrogen and the anthraquinone π-system,[46] facilitating delocalization of charge carriers across the polymer backbone and imparting superior electron-transport characteristics. The sole O 1s component at 532.4 eV (Fig. S2) is ascribed to carbonyl oxygen (C=O) within the quinonoid rings.

FTIR spectra of AAQ and PAAQ are displayed in Fig. 2d. For the monomer, the symmetric and asymmetric N–H stretching vibrations of the terminal $-NH_2$ group are observed at 3420 and 3300 cm^{-1}, respectively.[47] After oxidative polymerization, these two peaks coalesce into a single broad envelope centered at 3470 cm^{-1}, confirming the conversion of $-NH_2$ into the –NH– group within the polymer backbone.[48] Additional spectral signatures can be summarized as follows: (1) a strong band at 1640 cm^{-1}, common to both AAQ and PAAQ, is ascribed to the C=O stretching vibration of the quinonoid carbonyl. (2) PAAQ

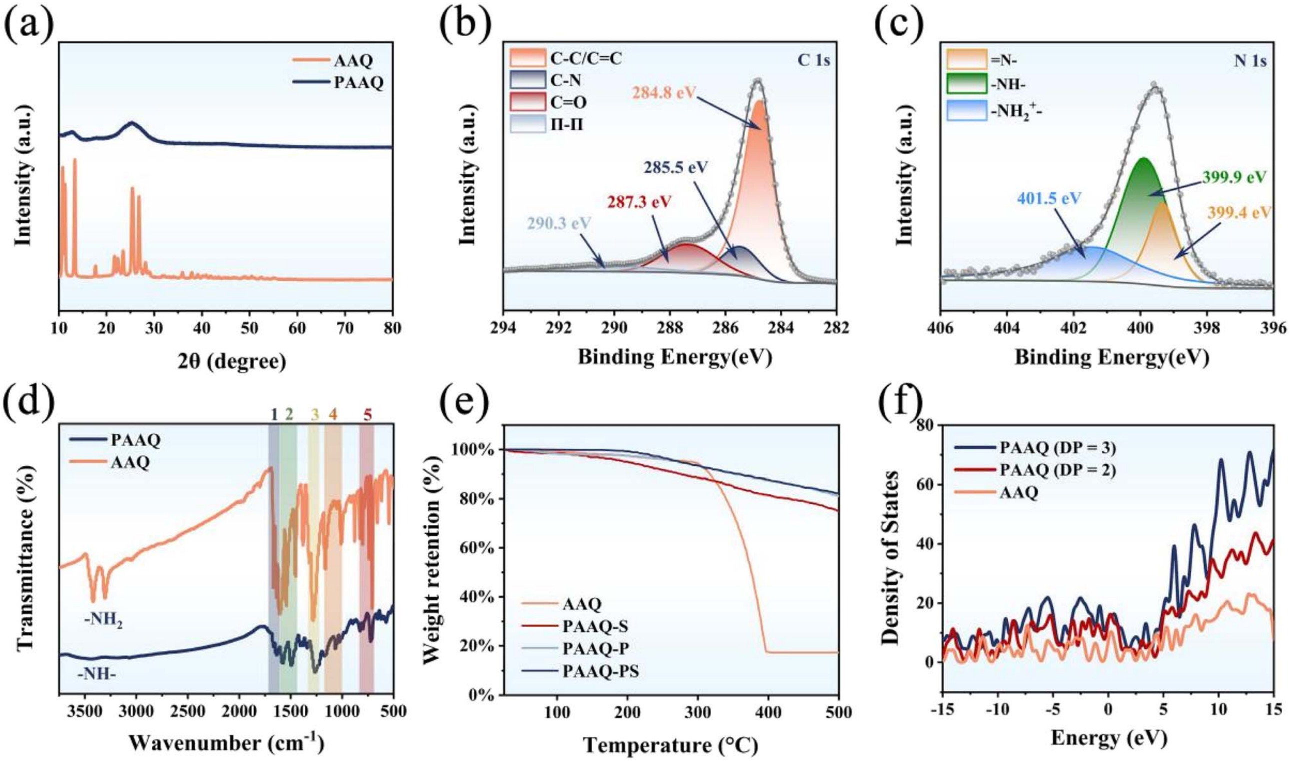

Fig. 2 (a) XRD patterns of PAAQ. High-resolution XPS spectra of (b) C 1s and (c) N 1s. (d) FTIR spectroscopy of AAQ and PAAQ. (e) TGA curve of samples. (f) The corresponding DOS for AAQ and PAAQ.

exhibits two well-resolved peaks at 1580 cm^{-1} and 1490 cm^{-1} that are attributed to in-plane skeletal vibrations of the quinonoid and benzenoid rings, respectively. In contrast, AAQ displays three broader and less-defined bands in the same region, reflecting the shorter effective conjugation length of the monomer.[49] (3) The aromatic C–N stretching mode at 1290 cm^{-1} in AAQ undergoes a red-shift to 1270 cm^{-1} in PAAQ, consistent with the formation of C–NH–C bridges upon polymerization.[50,51] (4) The series of bands between 1180 and 1010 cm^{-1} originate from in-plane C–H deformation modes. (5) Out-of-plane bending vibrations appear at 827 and 800 cm^{-1} (two adjacent C–H) and 723 and 710 cm^{-1} (three adjacent C–H) on the benzene ring. FTIR spectra of the control samples (Fig. S3) demonstrate that PAAQ-S retains most of the characteristic peaks of AAQ, including the free $-NH_2$ stretches, corroborating the incomplete polymerization in the absence of protic acid. Conversely, PAAQ-P exhibits spectral features nearly identical to those of PAAQ, indicating that mechanical stirring influences microstructure rather than the intrinsic chemical functionality of the polymer.

TGA demonstrates a pronounced improvement in thermal stability upon polymerization (Fig. 2e). PAAQ exhibits negligible mass loss below 200 °C and shows >90% weight retention at 300 °C. The subsequent degradation is also very slow, and PAAQ-S may exhibit slightly weaker thermal stability than the other two polymerization products due to incomplete polymerization. In stark contrast, the AAQ monomer undergoes catastrophic decomposition above 300 °C, retaining merely 20% of its initial mass at 400 °C. These results attest to the robustness of the polymer backbone. Variations in the density of states (DOS) at the Fermi level occurring in the pores of AAQ and PAAQ (polymerization degree = 2, 3) were further investigated by using VASP AIMD simulations (Fig. 2f). The results indicate that the formation of a more complete π-conjugated framework through further polymerization reaction may enhance the density of states on the material surface, which is expected to promote the transfer of electrons on the polymer chain and enhance the overall conductivity of the material.[52] N_2 sorption isotherms and pore-size distributions of the four samples are presented in Fig. S5. According to the IUPAC classification,[53] both PAAQ and PAAQ-P exhibit type IV isotherms (Fig. S4a). A gradual uptake at low-to-intermediate relative pressures (p/p_0 < 0.4) indicates a lack of micropore structure, whereas a pronounced capillary condensation step accompanied by a clear H_3-type hysteresis loop at p/p_0 > 0.8 is diagnostic of a mesopore/macropore network. This feature is more pronounced for PAAQ-P. The corresponding BJH pore-size distributions (Fig. S4b) corroborate the predominance of mesopores (2–50 nm) and macropores (>50 nm) in all polymerized products. BET analysis yields the following SSAs: PAAQ-S (27.59 $m^2\ g^{-1}$) > PAAQ-PS (19.53 $m^2\ g^{-1}$) > PAAQ-P (15.35 $m^2\ g^{-1}$) > AAQ (2.67 $m^2\ g^{-1}$). For applications of electrode materials, a higher SSA shortens ion-diffusion pathways, enhances charge-storage capacity and improves adsorption kinetics. Notably, all polymeric products possess markedly larger SSAs than the AAQ monomer, ensuring abundant electroactive sites. The exceptionally high SSA of PAAQ-S originates from its fragmented, incompletely polymerization morphology. But this morphological characteristic does not necessarily translate to superior electrosorption performance. Conversely, the quiescent interfacial polymerization of PAAQ-P yields a compact, agglomerated architecture, resulting in the lowest SSA among the polymers.

3.2. Electrochemical characterization

The various organic electrodes were characterized by a conventional three-electrode configuration (Fig. S5–S8). Cyclic voltammetry (CV) and galvanostatic charge–discharge (GCD) curves (Fig. 3a and b) reveal a quasi-reversible redox couple for both PAAQ-PS and PAAQ-P, which can be attributed to the enolization of C═O to C–OH on the anthraquinone core.[54,55] This transformation confirms that PAAQ possesses redox-active sites capable of NH_4^+ storage. Notably, the redox peak is close to zero potential, indicating facile activation of these sites.[56] In contrast, both PAAQ-S and AAQ exhibit almost pure electrical double layer behavior at higher scanning rates, with only weak and far from zero potential redox signals observed at scanning rates below 10 mV s^{-1} (Fig. S7f) and 1 mV s^{-1} (Fig. S8h), respectively. These observations corroborate that C═O on the conjugated backbone is intrinsically redox-active. P-doping of the PAAQ chain owing to the protonation of –NH– triggers an extensive delocalization of the π-electron cloud across the anthraquinone scaffold, thereby expanding the π-conjugated structure and markedly optimizing the energy bandgap and electronic properties.[57,58] Consequently, the redox-active sites are electronically activated,[59] manifesting as a pronounced decrease in the redox potential and substantial increase in integrated peak area. Although PAAQ-S bears a comparatively weak π-system, its CV and GCD curves display lower polarization than those of monomeric AAQ (Fig. S7a, b, S8a and b), underscoring that a low degree of π-conjugation can still provide minor additional capacitance performance. As shown in Fig. 3c, the specific capacitance of different electrode materials measured at 0.5 A g^{-1} is in the order: PAAQ-PS (203.95 F g^{-1}) > PAAQ-P (160.73 F g^{-1}) > PAAQ-S (56.65 F g^{-1}) > AAQ (11.2 F g^{-1}). The superior performance of PAAQ-PS relative to PAAQ-P stems from the stirring operation during the polymerization process, which possibly suppresses excessive π–π stacking of the polymer chains under static conditions, optimizing charge distribution and extending further electron delocalization.[56] In contrast, the pronounced advantage of PAAQ-PS over both PAAQ-S and AAQ originates from the post-protonation expansion of π-conjugation, which simultaneously unlocks latent redox activity and cooperatively amplifies ion-storage capacity. Overall, the above results demonstrate that the strategy of protonation to regulate electron delocalization possibly exerts a more decisive influence on capacitance of PAAQ than do structural modifications.

To gain deeper insight into the capacitive response of organic electrode materials, the fraction of diffusion-controlled capacitance was quantified (Fig. 3d). The theory proposed by Duun *et al.* can be used to quantitatively calculate the ratio of current generated by diffusion control and capacitance control at a certain scanning rate: $i = k_1\nu + k_2\nu^{0.5}$, where $k_1\nu$ and $k_2\nu^{0.5}$

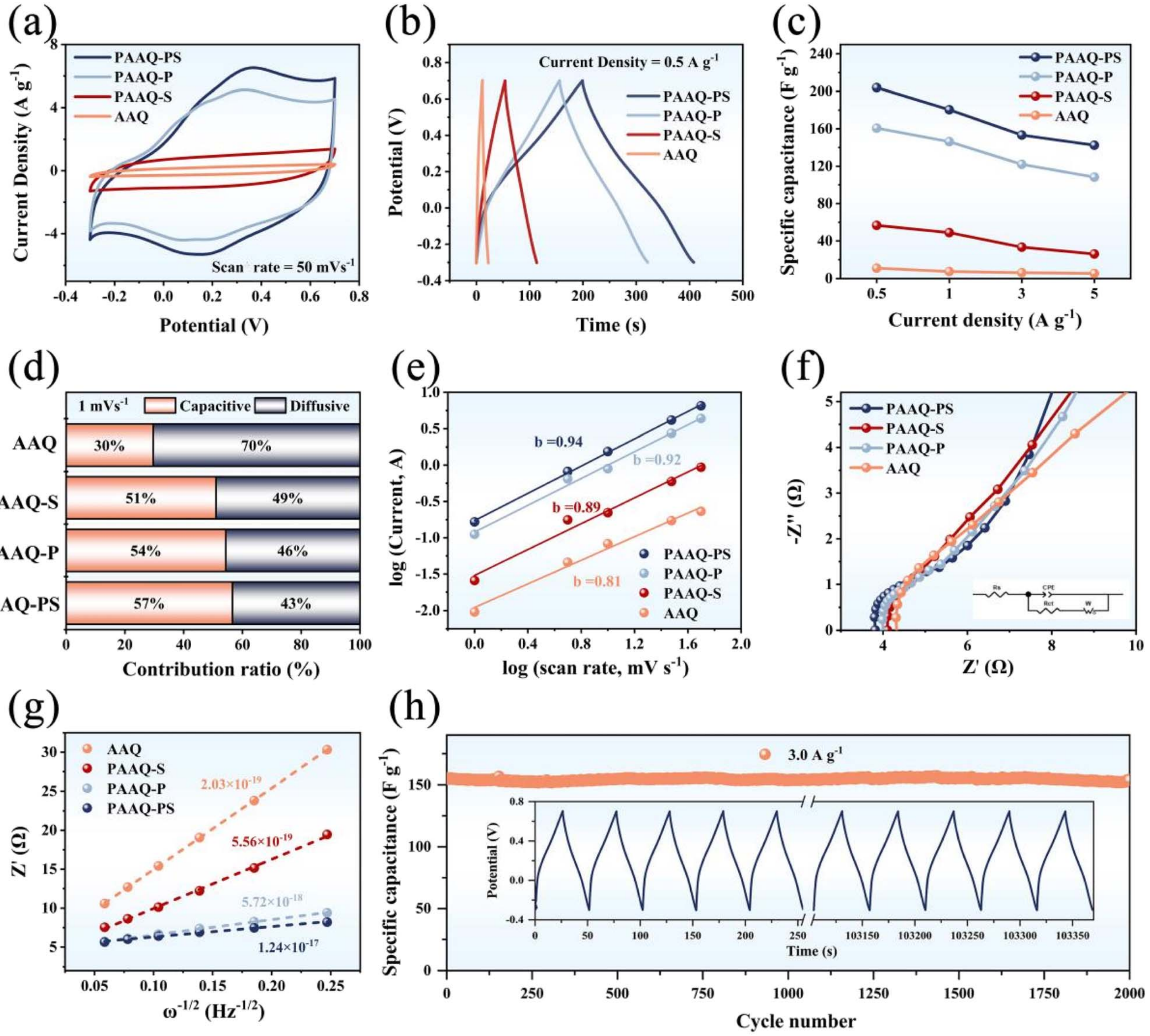

Fig. 3 (a) CV and (b) GCD curves of various organic electrodes in 1 M NH_4Cl solution. (c) GCD specific capacitances, (d) contribution of capacitance and diffusion control capacity, (e) power-law relationship between oxidation peak current and scan rate of organic electrodes. (f) Nyquist plot of organic electrodes and equivalent circuit diagram. (g) NH_4^+ diffusion coefficient of organic electrodes. (h) Long-term cycling performance and corresponding GCD curves of the PAAQ electrode at 3 A g^{-1}.

represent surface capacitance control current and diffusion control current, respectively.[60] Owing to the rapid surface-capacitive kinetics imparted by the wider range of electron delocalized π-conjugated skeleton, the quinone-based electrodes in this work exhibit a markedly higher capacitive contribution than most previously documented organic or ammonium-selective electrodes.[30,34,54,61,62] At the scan rate of 1 mV s^{-1}, the capacitive ratios are 30% for AAQ, 51% for PAAQ-S, 54% for PAAQ-P, and 57% for PAAQ-PS. These imply that the proportion of capacitance control is possibly governed predominantly by the extended π-conjugation which emerges after polymerization, whereas redox sites exert a secondary influence. Among these, PAAQ-PS presents the largest capacitive proportion, indicating its superior applicability for rapid storage of NH_4^+. A power-law analysis correlating the current response with scan rate was performed based on the CV results. Typically, dynamics of the electrode are divided into capacitance control and diffusion control. The scan rate (v) *versus* current (i) relationship follows a power-law dependence, $i = av^b$, where a and b are adjustable parameters obtained from the linear fitting of $\log i$ *versus* $\log v$. The b-value of 0.5 indicates that diffusion-controlled reactions dominate, while a b-value of 1.0 indicates complete capacitive behavior.[63] The b-values of four organic materials were obtained by calculating the currents of the oxidation peak and reduction peak at different scan rates (Fig. S5–S8i). Notably, a certain difference in b-values is observed between PAAQ-PS and PAAQ-P, while PAAQ-S and AAQ have almost no such phenomenon, especially AAQ. Combined with the slight asymmetry of the CV curves, this indicates that the additional enolization mechanism does not conform to a simple reversible kinetic relationship possibly. Fig. 3e presents the *b*-values derived from the anodic peak currents of all four materials. *b*-Values approaching 1.0 for the three polymer electrodes signify that dynamics is governed predominantly by capacitive processes, corroborating the quantitative capacitive-diffusion contribution analysis.

Electrochemical impedance spectroscopy (EIS) measurements yielded the Nyquist plot presented in Fig. 3f. The high-frequency intercept and semicircle diameter represent the solution resistance (R_s) and charge-transfer resistance (R_{ct}), respectively. Fitted values follow the sequence R_s: PAAQ-PS (3.81 Ω) < PAAQ-P (4.01 Ω) < PAAQ-S (4.10 Ω) < AAQ (4.33 Ω); R_{ct}: PAAQ-PS (3.14 Ω) < PAAQ-P (5.85 Ω) < PAAQ-S (6.88 Ω) < AAQ (15.49 Ω). The exceptionally low R_s and R_{ct} of PAAQ-PS are ascribed to the electron delocalization of its polymer chains and optimized surface-charge distribution in a rice-grain morphology, which facilitate rapid electron/ion transport and enhance redox kinetics.[35] The Warburg coefficient (R_w), derived from the low-frequency linear region, decreases in the order PAAQ-PS < PAAQ-P < PAAQ-S < AAQ, corroborating the smallest R_w for PAAQ-PS.[64] Consequently, based on eqn (2), the NH_4^+ diffusion coefficient (Fig. 3g) is highest for PAAQ-PS (1.2×10^{-17}), affirming its superior pseudocapacitive behavior. Cycling stability was evaluated by GCD cycling at 3.0 A g^{-1}. Over 2000 cycles, PAAQ-PS exhibited negligible capacitance fade (Fig. 3h), underscoring its outstanding electrochemical reversibility. The organic pseudocapacitive material's robustness is attributed to its reliance on functional groups as redox-active sites for ion adsorption, in contrast to storage mechanisms involving phase transitions. This property enables it to circumvent issues like the substantial volume expansion observed in many inorganic materials, while preserving excellent structural integrity throughout extended cycling.

3.3. CDI performance evaluation

To evaluate the efficiency of the HCDI system for NH_4^+ removal, adsorption experiments were conducted by using a custom-built CDI device. As showed in Fig. 4a, the device was configured with the PAAQ electrode material as the cathode for adsorbing NH_4^+, and commercially available activated carbon as the anode for adsorbing Cl^-. Upon reversing the voltage, the ions adsorbed on the electrode were desorbed, and the electrode achieves regeneration. To prevent the capture of ions during voltage reversal, an anion exchange membrane (AEM) and a cation exchange membrane (CEM) were positioned adjacent to the anode and cathode surfaces, respectively. During the process of increasing the applied voltage from 0.8 V to 1.2 V, the specific adsorption capacity of organic electrodes for NH_4^+ significantly increased, indicating that high voltage helps enhance the deionization ability of HCDI devices (Fig. 4b). Adsorption capacities toward NH_4^+ at 1.2 V were calculated using eqn (3) and followed the order: PAAQ-PS (120.43 mg g^{-1}) > PAAQ-P (100.52 mg g^{-1}) > PAAQ-S (70.83 mg g^{-1}) > AAQ (17.13 mg g^{-1}) (Fig. 4b), a trend that mirrors the preceding electrochemical metrics. The highest specific capacitance observed for PAAQ-PS translates into the best NRC. The Ragone

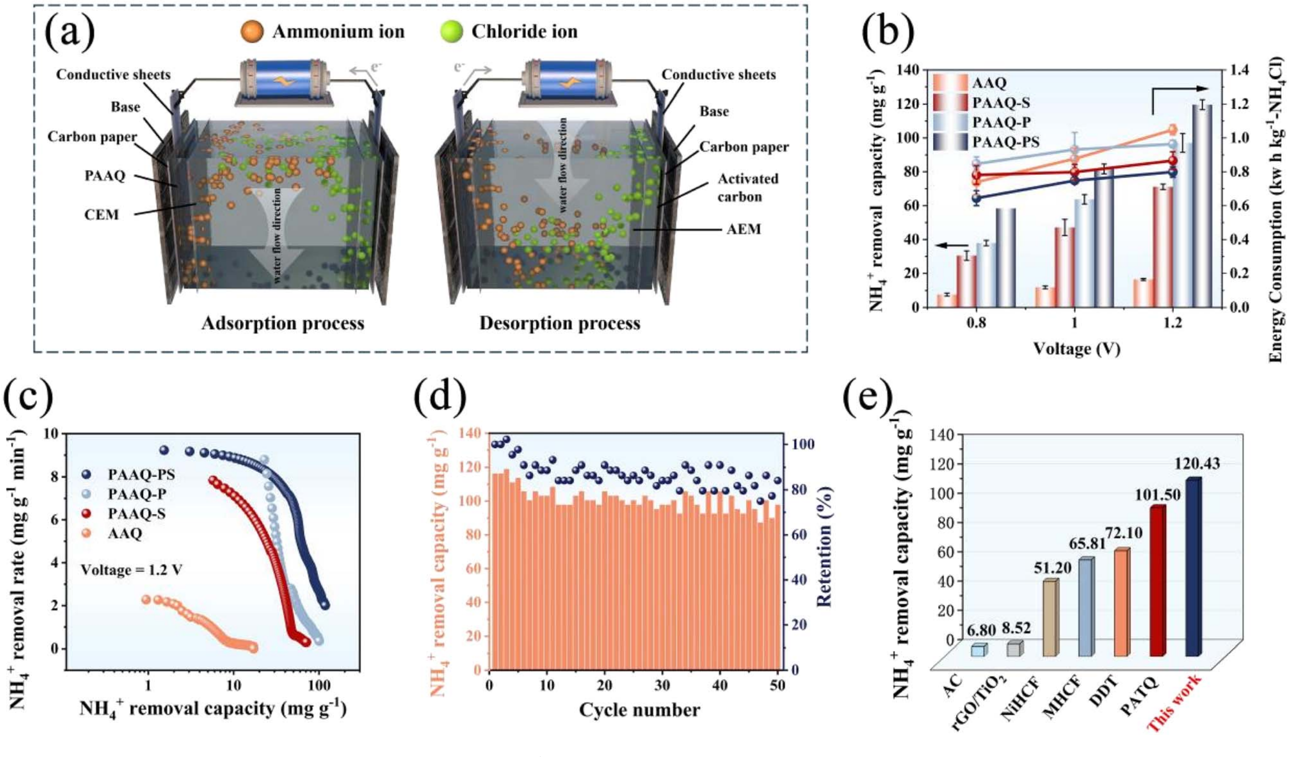

Fig. 4 (a) Schematic of the PAAQ//AC HCDI process. NH_4^+ removal capacity, energy consumption (b) and Ragone plots (c) of PAAQ under various voltages. (d) Cycling performances and retention values of PAAQ electrodes at 1.2 V. (e) NH_4^+ removal capacity comparison of other electrode materials.

plot (Fig. 4c) shows that the PAAQ-PS electrode shifts furthest toward the upper-right quadrant, evidencing simultaneously elevated NRC and NRR. A high NRR of 9.23 mg g^{-1} min^{-1} was achieved by the HCDI device during the initial adsorption phase under 1.2 V operation. Attributed to its rapid surface redox reaction, the performance surpasses that of polymers obtained through previous synthetic methods of AAQ.[55] Combined with the result of the electrochemical test, the adsorption performance gain is ascribed to the global upshift in electronic conductivity coupled with judicious microstructure optimization, highlighting the advantages of the protonation regulation and interfacial polymerization approach.

Conversely, the bulky morphology of PAAQ-P induces steric shielding of redox-active moieties and excessive π–π stacking, both of which impede interfacial charge transfer and yield a marginally lower NRC than the rice-shaped PAAQ-PS. These observations underscore the potential of morphology engineering for low-crystallinity organic frameworks whose architectures are highly tunable. PAAQ-S suffers from a poor-continuity π-conjugated network due to lack of polarization induced electron delocalization. Although it possesses the highest SSA, restricted electron mobility prevents full activation of surface redox sites, thereby diminishing NH_4^+ adsorption. Nevertheless, its capacity still exceeds that of pristine AAQ, confirming that the partially conjugated segments generated by moderate polymerization do facilitate electron transport. Relative to PAAQ synthesized under acidic conditions, however, a pronounced performance gap persists, highlighting the pivotal role of a well-developed π-conjugated framework in achieving superior NH_4^+ capture. A critical factor in judging CDI electrode performance is their long-term stability. To determine the reversibility and cycling stability of PAAQ electrodes within a CDI device, cycling performance was assessed in a 1.2 V NH_4Cl solution (Fig. 4d). After 50 cycles, the NRC of PAAQ-PS was maintained at 84.1% of its initial value, confirming its satisfactory cycling stability. Compared to previous ammonium removal electrode materials, PAAQ-PS exhibits good adsorption capacity (Fig. 4e).[23,24,54,55,65,66]

3.4. Ionic deintercalation mechanism

To elucidate the NH_4^+ storage mechanism of PAAQ, *ex situ* XPS was performed on the PAAQ-PS electrode before and after CDI (Fig. 5a). The O 1s spectra reveal that only a C=O component at 532.4 eV is present prior to CDI. After NH_4^+ uptake, the C=O peak attenuates concomitantly with the emergence of a new C–OH feature at 533.7 eV. This spectral evolution corroborates the enolization of quinonyl C=O moieties to C–OH, thereby enabling reversible NH_4^+ storage (Fig. 5b), in agreement with prior studies.[54,55] Specifically, a negative voltage is applied to the PAAQ electrode during the CDI adsorption step. The C=O on

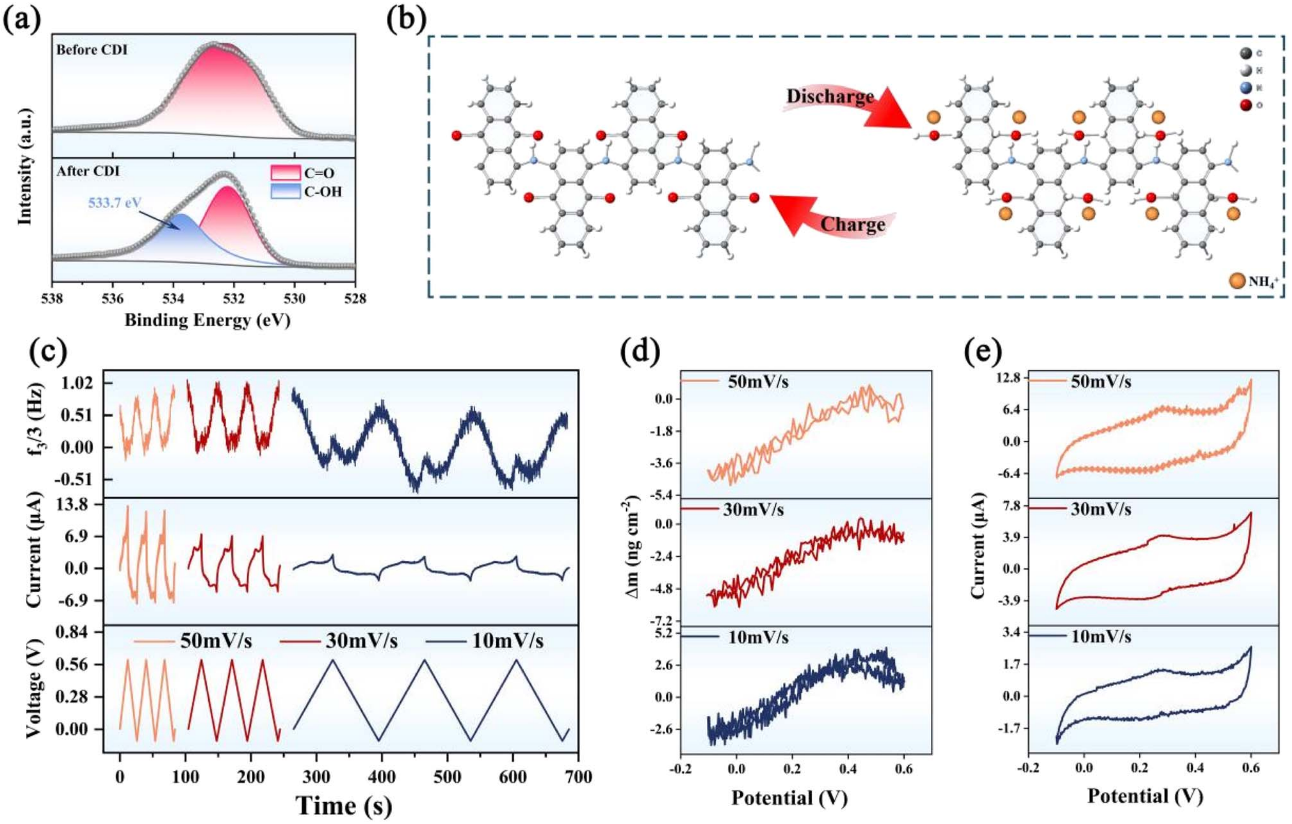

Fig. 5 (a) High-resolution XPS spectra of O 1s for PAAQ before and after CDI. (b) Structural evolutions of PAAQ upon enolization for NH_4^+ uptake/removal. (c) Time-dependent changes in $\Delta f_3/3$, current and voltage of PAAQ at different scan rates measured *via* EQCM. The corresponding mass change (d) and current change (e) of PAAQ at various scan rates.

the PAAQ backbone is reduced to C–OH. This reduction imparts a stronger electronegativity to the oxygen atom, enabling it to bind NH_4^+ through hydrogen bonding or chelation, thereby forming a C–OH–NH_4^+ structure. This additional binding mode increases the upper limit of NH_4^+ adsorption. When the voltage is inverted, the C–OH groups are oxidized back to C═O. This transformation weakens the affinity for NH_4^+, and together with the electrostatic repulsion from the positive potential, NH_4^+ is efficiently released from the electrode. The electrodes of PAAQ-P, PAAQ-S, and AAQ after CDI were further tested by XPS (Fig. S9). Only PAAQ-P mirrors the behavior of PAAQ-PS, exhibiting a pronounced enolization signature through the appearance of C–OH functionalities alongside attenuated C═O signals. In contrast, PAAQ-S and AAQ retain their original C═O profiles after CDI, owing to their incomplete π-conjugation, which precludes activation of the quinone redox centers. This spectroscopic evidence is consistent with the electrochemical results.

To further quantify ionic fluxes during adsorption/desorption, EQCM-D was coupled with cyclic voltammetry. Fig. 5c shows that, during the anodic sweep at progressively lower scan rates, the normalized frequency shift ($\Delta f_3/3$) decreases stepwise, signifying Cl^- adsorption and a concomitant increase in PAAQ mass. Upon cathodic polarization, Cl^- is expelled while NH_4^+ is incorporated. The overall mass declines because the molar mass of desorbed Cl^- exceeds that of adsorbed NH_4^+. Notably, the transition from anodic to cathodic polarization induces a transient frequency reversal: the mass initially rises slightly before monotonically decreasing. This effect intensifies at slower scan rates, suggesting a diffusion-limited enolization of residual C═O groups that facilitates additional NH_4^+ uptake, potentially exceeding the mass loss from Cl^- release. The closed Δm–potential hysteresis loop in Fig. 5d demonstrates the robust cyclability of PAAQ under repeated redox behavior. Although the net mass loss per cycle is negligible, it is evident that as the scan rate decreases, the magnitude of mass change within a single cycle increases significantly. This observation indicates that at lower scan rates, ions have sufficient time to diffuse fully into the interior of the electrode material, thereby enabling more pronounced mass variation. Moreover, the lower scan rate accentuates the mass reversal phenomenon, that is, the transient frequency reversal around the potential switching point, further demonstrating that the enolization-driven pseudocapacitive effect is more fully realized under slower kinetic conditions.

Fig. 5e displays the CV recorded simultaneously with the EQCM-D measurements. Although a well-defined redox couple is still discernible, its formal potentials are displaced further from zero potential point relative to those observed in conventional CV performed on coated electrodes. This shift may be ascribed to the higher degree of dispersion of the electroactive film on the quartz-crystal chip, which disrupts the π–π stacking that normally endows conjugated polymers with their certain electrochemical characteristics.[56] Taking the scan rate of 10 mV s^{-1} as representative, the potential at which the mass transition changes from an initial increase to a subsequent decrease, as illustrated in Fig. 5d, coincides almost exactly with the cathodic peak potential in the CV. This correspondence demonstrates that, once the applied potential falls below this value, enolization-driven NH_4^+ uptake by PAAQ ceases. Consequently, the expulsion of Cl^- and the sorption of NH_4^+ reach a dynamic equivalence in molar terms, manifesting as a net decrease in the overall electrode mass.

4. Conclusion

In summary, this work successfully prepared PAAQ nanomaterials with abundant redox active sites and appreciable electronic conductivity through a mild strategy combining protonation and interfacial polymerization. This method effectively solved the problem of insufficient active sites and slow adsorption rate caused by diffusion control in traditional organic materials. PAAQ-PS demonstrates significantly enhanced NH_4^+ adsorption performance over both the non-acid-mediated PAAQ-S and the statically polymerized PAAQ-P. This advantage arises from its combination of improved conductivity, due to electron delocalization from –NH_2^+– polarons, and a morphology that facilitates the exposure of redox-active sites. The experimental results showed that under a voltage of 1.2 V, the adsorption capacity of PAAQ for NH_4^+ reached 120.43 mg g^{-1}, with an adsorption rate of 9.22 mg g^{-1} min^{-1}, and it could still maintain 84.1% of the initial adsorption capacity after 50 cycles, demonstrating excellent cycling stability and rapid adsorption ability. This study provides innovative ideas for activating the redox active sites of organic conjugated polymers to enhance their adsorption capacity, further promoting the application and development of CDI technology in the fields of NH_4^+ removal and resource recovery.

Conflicts of interest

There are no conflicts to declare.

Data availability

The data that support the findings of this study will be shared upon reasonable request to the corresponding author.

Supplementary information (SI) is available. See DOI: https://doi.org/10.1039/d6ta02416e.

Acknowledgements

This research is supported by the National Natural Science Foundation of China (22276137, 22576153), Tianshan Innovation Team of Xinjiang Uygur Autonomous Region (2025D14023), and Outstanding Youth Science Fund Project of Xinjiang Uygur Autonomous Region (2025D01E22). This work was funded by the Xinjiang Leading Talent Program (XJRC-2025-KJ-YJ-CXPT-214) and the Xinjiang Key Laboratory of Engineering Materials and Structural Safety Open Science Project (XKLEMSS2025B07).

References

1 Q. C. Xu, S. X. Wang, J. K. Jiang, N. Bhattarai, X. X. Li, X. Chang, X. H. Qiu, M. Zheng, Y. Hua and J. M. Hao, Nitrate dominates the chemical composition of $PM_{2.5}$ during haze event in Beijing, China, *Sci. Total Environ.*, 2019, **689**, 1293–1303.

2 Z. P. Zhao, B. Wang, Q. W. Feng, M. Chen, X. Y. Zhang and R. H. Zhao, Recovery of nitrogen and phosphorus in wastewater by red mud-modified biochar and its potential application, *Sci. Total Environ.*, 2023, **860**, 15.

3 J. K. Song, X. Zhao, R. R. Liu, Y. H. Wang, D. Y. Zhu, X. Y. Wang, K. Jiang and D. P. Wu, Simultaneous removal and recovery of ammonium and phosphate ions using flow electrode capacitive deionization through the struvite generation mechanism, *Sep. Purif. Technol.*, 2025, **358**, 11.

4 T. Cai, D. Zhao and E. Gutmark, Overview of fundamental kinetic mechanisms and emission mitigation in ammonia combustion, *Chem. Eng. J.*, 2023, **458**, 17.

5 M. Van Damme, L. Clarisse, S. Whitburn, J. Hadji-Lazaro, D. Hurtmans, C. Clerbaux and P. F. Coheur, Industrial and agricultural ammonia point sources exposed, *Nature*, 2018, **564**, 99–103.

6 Q. Q. Yin, R. K. Wang and Z. H. Zhao, Application of Mg-Al-modified biochar for simultaneous removal of ammonium, nitrate, and phosphate from eutrophic water, *J. Clean. Prod.*, 2018, **176**, 230–240.

7 P. M. Glibert, F. P. Wilkerson, R. C. Dugdale, J. A. Raven, C. L. Dupont, P. R. Leavitt, A. E. Parker, J. M. Burkholder and T. M. Kana, Pluses and minuses of ammonium and nitrate uptake and assimilation by phytoplankton and implications for productivity and community composition, with emphasis on nitrogen-enriched conditions, *Limnol. Oceanogr.*, 2016, **61**, 165–197.

8 Y. M. Yang, B. B. Tao, C. H. Liu, M. H. Li, W. J. Wu, Y. Y. She, J. Zhang, H. K. Thabet, M. H. Helal, Z. M. El-Bahy and X. T. Xu, Capacitive deionization for ammonia recovery: progresses and challenges, *Chem. Eng. J.*, 2024, **500**, 21.

9 P. P. Li, Z. Y. Jin, Z. W. Fang and G. H. Yu, A single-site iron catalyst with preoccupied active centers that achieves selective ammonia electrosynthesis from nitrate, *Energy Environ. Sci.*, 2021, **14**, 3522–3531.

10 J. Choi, B. H. R. Suryanto, D. B. Wang, H. L. Du, R. Y. Hodgetts, F. M. F. Vallana, D. R. MacFarlane and A. N. Simonov, Identification and elimination of false positives in electrochemical nitrogen reduction studies, *Nat. Commun.*, 2020, **11**, 10.

11 A. Valera-Medina, F. Amer-Hatem, A. K. Azad, I. C. Dedoussi, M. de Joannon, R. X. Fernandes, P. Glarborg, H. Hashemi, X. He, S. Mashruk, J. McGowan, C. Mounaim-Rouselle, A. Ortiz-Prado, A. Ortiz-Valera, I. Rossetti, B. Shu, M. Yehia, H. Xiao and M. Costa, Review on Ammonia as a Potential Fuel: From Synthesis to Economics, *Energy Fuels*, 2021, **35**, 6964–7029.

12 H. Cruz, Y. Y. Law, J. S. Gues, K. Rabaey, D. Batstone, B. Laycock, W. Verstraete and I. Pikaar, Mainstream Ammonium Recovery to Advance Sustainable Urban Wastewater Management, *Environ. Sci. Technol.*, 2019, **53**, 11066–11079.

13 M. R. Adam, M. H. D. Othman, R. A. Samah, M. H. Puteh, A. F. Ismail, A. Mustafa, M. A. Rahman and J. Jaafar, Current trends and future prospects of ammonia removal in wastewater: a comprehensive review on adsorptive membrane development, *Sep. Purif. Technol.*, 2019, **213**, 114–132.

14 M. S. Miah, N. Amjady, R. Shah and S. Islam, Energy Recovery From Polluted Water Using Capacitive Deionization Desalination System: A Review, *IEEE Access*, 2024, **12**, 110002–110027.

15 M. J. Liu, M. Y. He, J. L. Han, Y. Y. Sun, H. Jiang, Z. Li, Y. N. Li and H. F. Zhang, Recent Advances in Capacitive Deionization: Research Progress and Application Prospects, *Sustainability*, 2022, **14**, 41.

16 J. Ma, R. H. Zhou and F. Yu, Hotspots and future trends of capacitive deionization technology: a bibliometric review, *Desalination*, 2024, **571**, 11.

17 J. Ma, C. X. Zhai and F. Yu, Review of flow electrode capacitive deionization technology: research progress and future challenges, *Desalination*, 2023, **564**, 21.

18 N. L. Liu, S. H. Sun and C. H. Hou, Studying the electrosorption performance of activated carbon electrodes in batch-mode and single-pass capacitive deionization, *Sep. Purif. Technol.*, 2019, **215**, 403–409.

19 S. Zhao, J. S. Fang, Y. Y. Wang, Y. W. Zhang, Y. M. Zhou and S. P. Zhuo, Construction of three-dimensional mesoporous carbon nitride with high surface area for efficient visible-light-driven hydrogen evolution, *J. Colloid Interface Sci.*, 2020, **561**, 601–608.

20 J. S. Kang, S. Kim, J. H. Kang, H. Joo, J. Jang, K. Jo, S. Park, H. I. Kim, S. J. Yoo, J. Yoon, Y. E. Sung and T. A. Hatton, Surface Electrochemistry of Carbon Electrodes and Faradaic Reactions in Capacitive Deionization, *Environ. Sci. Technol.*, 2022, **56**, 12602–12612.

21 D. Lu, W. F. Cai and Y. Wang, Optimization of the voltage window for long-term capacitive deionization stability, *Desalination*, 2017, **424**, 53–61.

22 T. K. A. Nguyen, N. T. N. Anh, M. D. Nguyen, V. T. Nguyen and R. A. Doong, Boosting capacitive deionization of monovalent and hardness ions using Ti3C2Tx MXene as an intercalation-type pseudocapacitive electrode, *Sep. Purif. Technol.*, 2023, **327**, 13.

23 S. W. Tsai, D. V. Cuong and C. H. Hou, Selective capture of ammonium ions from municipal wastewater treatment plant effluent with a nickel hexacyanoferrate electrode, *Water Res.*, 2022, **221**, 10.

24 Q. F. Wang, Q. H. Wu, S. J. Meng, H. J. Liu and D. W. Liang, Selective removal of ammonium ions with transition metal hexacyanoferrate (MHCF) electrodes, *Desalination*, 2023, **558**, 9.

25 S. Q. Gong, H. B. Liu, F. Zhao, Y. N. Zhang, H. T. Xu, M. Li, J. J. Qi, H. H. Wang, C. L. Li, W. C. Peng, X. B. Fan and J. P. Liu, Vertically Aligned Bismuthene Nanosheets on

MXene for High-Performance Capacitive Deionization, *ACS Nano*, 2023, **17**, 4843–4853.

26 J. Yang, W. X. Hou, R. Pan, M. Zhou, S. Z. Zhang and Y. Zhang, The interfacial electronic engineering in polyhedral MOF derived Co-doped $NiSe_2$ composite for upgrading rate and longevity performance of aqueous energy storage, *J. Alloys Compd.*, 2022, **897**, 7.

27 Y. Lu, Q. Zhang, L. Li, Z. Q. Niu and J. Chen, Design Strategies toward Enhancing the Performance of Organic Electrode Materials in Metal-Ion Batteries, *Chem*, 2018, **4**, 2786–2813.

28 T. Sun, J. Xie, W. Guo, D. S. Li and Q. C. Zhang, Covalent-Organic Frameworks: Advanced Organic Electrode Materials for Rechargeable Batteries, *Adv. Energy Mater.*, 2020, **10**, 23.

29 J. J. Shea and C. Luo, Organic Electrode Materials for Metal Ion Batteries, *ACS Appl. Mater. Interfaces*, 2020, **12**, 5361–5380.

30 Y. H. Tao, Y. J. Cui, H. X. Wang, Z. L. Li, Z. J. S. Qian, P. P. Zhang, H. J. Zhou and M. J. Shi, High-Efficiency Electrochemical Desalination: The Role of a Rigid Pseudocapacitive Polymer Electrode with Diverse Active Sites, *Adv. Funct. Mater.*, 2025, **35**, 11.

31 Z. Y. Zhuang, L. Sun, Y. H. Tao, J. Shao, J. G. Yang, P. Yu, H. X. Chen, J. H. Zhou, J. Xiao, K. Y. Yin, M. J. Shi and P. Xiao, Highly Efficient and Stable Capacitive Deionization Based on a Flower-Like Conjugated Polymer with Double Active-Sites, *Energy Environ. Mater.*, 2024, **8**, 9.

32 M. Quan, D. Sanchez, M. F. Wasylkiw and D. K. Smith, Voltammetry of quinones in unbuffered aqueous solution: reassessing the roles of proton transfer and hydrogen bonding in the aqueous electrochemistry of quinones, *J. Am. Chem. Soc.*, 2007, **129**, 12847–12856.

33 B. Schoepp-Cothenet, R. van Lis, A. Atteia, F. Baymann, L. Capowiez, A. L. Ducluzeau, S. Duval, F. t. Brink, M. J. Russell and W. Nitschke, On the universal core of bioenergetics, *Biochim. Biophys. Acta, Bioenerg.*, 2013, **1827**, 79–93.

34 R. W. Jing, J. Yang, X. R. Zhao, Y. T. Wang, P. R. Shao, M. J. Shi and C. Yan, A carbonyl-rich conjugated organic compound for aqueous rechargeable Na plus storage with wide voltage window workability, *J. Colloid Interface Sci.*, 2024, **658**, 678–687.

35 R. W. Jing, J. He, L. T. Hu, J. Yang, C. Yan and M. J. Shi, A holomolecule conjugated and electron delocalized organic compound for superior proton-storage redox capability, *Chem. Eng. J.*, 2023, **477**, 9.

36 Y. Y. Ding, X. Ren, D. Chen, F. J. Wen, T. Li and F. Xu, Poly(1,5-diaminoanthraquinone) as a High-Capacity Bipolar Cathode for Rechargeable Magnesium Batteries, *ACS Appl. Energy Mater.*, 2022, **5**, 3004–3012.

37 X. G. Li, X. L. Ma and M. R. Huang, Lead(II) ion-selective electrode based on polyaminoanthraquinone particles with intrinsic conductivity, *Talanta*, 2009, **78**, 498–505.

38 T. Günther, K. Oka, S. Olsson, M. Åhlén, N. Tohnai and R. Emanuelsson, Redox-site accessibility of composites containing a 2D redox-active covalent organic framework: from optimization to application, *J. Mater. Chem. A*, 2023, **11**, 13923–13931.

39 Z. Y. Meng, Y. Zhang, M. Q. Dong, Y. Zhang, F. M. Cui, T. P. Loh, Y. H. Jin, W. Zhang, H. S. Yang and Y. Du, Readily useable bulk phenoxazine-based covalent organic framework cathode materials with superior kinetics and high redox potentials, *J. Mater. Chem. A*, 2021, **9**, 10661–10665.

40 M. R. Huang, S. J. Huang and X. G. Li, Facile Synthesis of Polysulfoaminoanthraquinone Nanosorbents for Rapid Removal and Ultrasensitive Fluorescent Detection of Heavy Metal Ions, *J. Phys. Chem. C*, 2011, **115**, 5301–5315.

41 F. L. Zhang, J. B. Fan and S. T. Wang, Interfacial Polymerization: From Chemistry to Functional Materials, *Angew. Chem., Int. Ed.*, 2020, **59**, 21840–21856.

42 W. H. Shi, X. Y. Liu, T. Q. Deng, S. Z. Huang, M. Ding, X. H. Miao, C. Z. Zhu, Y. H. Zhu, W. X. Liu, F. F. Wu, C. J. Gao, S. W. Yang, H. Y. Yang, J. N. Shen and X. H. Cao, Enabling Superior Sodium Capture for Efficient Water Desalination by a Tubular Polyaniline Decorated with Prussian Blue Nanocrystals, *Adv. Mater.*, 2020, **32**, 9.

43 J. Jin, R. Y. Wang, K. Yu, Y. H. Tao, P. P. Zhang, L. Ke, J. Yang and M. J. Shi, Imine-based conjugated polymer enables efficient removal of ammonium ion via capacitive deionization, *Sep. Purif. Technol.*, 2025, **353**, 9.

44 D. D. Chen, X. H. Yi, C. Zhao, H. F. Fu, P. Wang and C. C. Wang, Polyaniline modified MIL-100(Fe) for enhanced photocatalytic Cr(VI) reduction and tetracycline degradation under white light, *Chemosphere*, 2020, **245**, 12.

45 T. Y. Liu, K. C. Kim, B. Lee, S. Jin, M. J. Lee, M. Li, S. Noda, S. S. Jang and S. W. Lee, Enhanced Lithium Storage of an Organic Cathode via the Bipolar Mechanism, *ACS Appl. Energy Mater.*, 2020, **3**, 3728–3735.

46 L. Lin, Z. R. Lin, J. Q. Zhu, K. Wang, W. L. Wu, T. Qiu and X. Q. Sun, A semi-conductive organic cathode material enabled by extended conjugation for rechargeable aqueous zinc batteries, *Energy Environ. Sci.*, 2023, **16**, 89–96.

47 J. L. Liu and P. Liu, Well-defined poly(1,5-diaminoanthraquinone)/reduced graphene oxide hybrids with superior electrochemical property for high performance electrochemical capacitors, *J. Colloid Interface Sci.*, 2019, **542**, 33–44.

48 S. J. Huang, C. G. Min, Y. Z. Liao, P. Du, H. Sun, Y. Q. Zhu and A. M. Ren, Intrinsically conducting polyaminoanthraquinone nanofibrils: interfacial synthesis, formation mechanism and lead adsorbents, *RSC Adv.*, 2014, **4**, 47657–47669.

49 A. I. Drachev, A. B. Gil'man and A. A. Kuznetsov, Polymerization of anthracene in a direct-current discharge, *High Energy Chem.*, 2005, **39**, 418–419.

50 J. L. Ren, X. Zhao, J. X. Zhang and Q. H. Zhang, Anthraquinone Immobilized on Reduced Graphene Oxide Sheets with Improved Electrochemical Properties for Supercapacitors, *Int. J. Electrochem. Sci.*, 2016, **11**, 2550–2559.

51 E. Jokar, S. Shahrokhian and A. I. Zad, Electrochemical functionalization of graphene nanosheets with catechol

derivatives as an effective method for preparation of highly performance supercapacitors, *Electrochim. Acta*, 2014, **147**, 136–142.

52 A. A. Zhang, Z. X. Wang, Z. B. Fang, J. L. Li and T. F. Liu, Long-Range π-π Stacking Brings High Electron Delocalization for Enhanced Photocatalytic Activity in Hydrogen-Bonded Organic Framework, *Angew. Chem., Int. Ed.*, 2024, **63**, 8.

53 P. P. Yu, Y. Z. Li, X. Y. Yu, X. Zhao, L. H. Wu and Q. H. Zhang, Polyaniline Nanowire Arrays Aligned on Nitrogen-Doped Carbon Fabric for High-Performance Flexible Supercapacitors, *Langmuir*, 2013, **29**, 12051–12058.

54 X. R. Zhao, J. Yang, J. Y. Peng, Y. Liu, H. Zhang, C. Yan and M. J. Shi, An extended S-heterocyclic organic compound with enhanced redox active sites for efficient and stable ammonium ion removal via capacitive deionization, *Desalination*, 2024, **592**, 11.

55 Y. H. Tao, J. Jin, X. Y. Zhang, Z. J. S. Qian, J. T. Jiang and M. J. Shi, A tailored polymer with enhanced electrosorption capability for efficient ammonium removal, *Sep. Purif. Technol.*, 2025, **362**, 8.

56 D. Jiang, R. B. Xu, L. Bai, J. P. Hill, J. Henzie, L. Y. Zhu, W. Xia, R. Bu, Y. J. Zhao, Y. Q. Kang, T. Hamada, R. Z. Ma, N. Torad, J. Wang, T. Asahi, X. T. Xu and Y. Yamauchi, Substrate Curvature-Induced Regulation of Charge Distribution of Covalent Organic Frameworks Promotes Capacitive Deionization, *Adv. Funct. Mater.*, 2024, **34**, 10.

57 R. Y. Wang, J. He, C. Yan, R. W. Jing, Y. Zhao, J. Yang, M. J. Shi and X. B. Yan, A Long-Range Planar Polymer with Efficient π-Electron Delocalization for Superior Proton Storage, *Adv. Mater.*, 2024, **36**, 12.

58 Q. Che, C. Y. Li, Z. H. Chen, S. Yang, W. F. Zhang and G. Yu, High Performance Memristors Based on Imine-Linked Covalent Organic Frameworks Obtained Using a Protonation Modification Strategy, *Angew. Chem., Int. Ed.*, 2024, **63**, 9.

59 J. He, Y. Zhao, C. Yan, R. W. Jing, R. Y. Wang and M. J. Shi, Highly redox-active polymer with extensive electron delocalization and optimized molecular orbitals for extraordinary proton storage, *Chem. Eng. J.*, 2023, **470**, 8.

60 T. Brezesinski, J. Wang, S. H. Tolbert and B. Dunn, Ordered mesoporous α-MoO_3 with iso-oriented nanocrystalline walls for thin-film pseudocapacitors, *Nat. Mater.*, 2010, **9**, 146–151.

61 R. Y. Wang, M. J. Shi, L. Y. Li, Y. Zhao, L. P. Zhao and C. Yan, In-situ investigation and application of cyano-substituted organic electrode for rechargeable aqueous Na-ion batteries, *Chem. Eng. J.*, 2023, **451**, 10.

62 Y. F. An, H. Zhang, D. X. Geng, Z. J. Fu, Z. M. Liu, J. He, Y. Zhao, M. J. Shi and C. Yan, Double redox-active polyimide-based covalent organic framework induced by lithium ion for boosting high-performance aqueous Zn^{2+} storage, *Chem. Eng. J.*, 2023, **477**, 9.

63 W. W. Ji, J. J. Niu, W. Zhang, X. Li, W. J. Yan, X. G. Hao and Z. D. Wang, An electroactive ion exchange hybrid film with collaboratively-driven ability for electrochemically-mediated selective extraction of chloride ions, *Chem. Eng. J.*, 2022, **427**, 11.

64 R. Vedalakshmi, V. Saraswathy, H. W. Song and N. Palaniswamy, Determination of diffusion coefficient of chloride in concrete using Warburg diffusion coefficient, *Corros. Sci.*, 2009, **51**, 1299–1307.

65 H. Sakar, O. Karatas, C. B. Canbolat, B. Keskinler and A. Karagunduz, Removal of ammonium ions by capacitive deionization and membrane capacitive deionization units, *Desalin. Water Treat.*, 2017, **75**, 260–267.

66 O. Pastushok, D. L. Ramasamy, M. Sillanpää and E. Repo, Enhanced ammonium removal and recovery from municipal wastewater by asymmetric CDI cell equipped with oxygen functionalized carbon electrode, *Sep. Purif. Technol.*, 2021, **274**, 13.